Geomorphology 182 (2013) 104–115

Contents lists available at SciVerse ScienceDirect

Geomorphology

journal homepage: www.elsevier.com/locate/geomorph

# Detection of subtle tectonic–geomorphic features in densely forested mountains by very high-resolution airborne LiDAR survey

Zhou Lin [a,b], Heitaro Kaneda [c,b,*], Sakae Mukoyama [d], Norichika Asada [d], Tatsuro Chiba [e]

[a] Department of Earth Sciences, Zhejiang University, China
[b] Active Fault and Earthquake Research Center, AIST, Geological Survey of Japan, Japan
[c] Department of Earth Sciences, Chiba University, Japan
[d] Kokusai Kogyo Co., Ltd., Japan
[e] Asia Air Survey Co., Ltd., Japan

ARTICLE INFO

*Article history:*
Received 6 July 2011
Received in revised form 12 September 2012
Accepted 1 November 2012
Available online 10 November 2012

*Keywords:*
Tectonic geomorphology
Airborne LiDAR
DEM
RRIM

ABSTRACT

Despite successes elsewhere in the world, 2 m resolution DEMs from a standard airborne LiDAR survey failed to detect small tectonic–geomorphic features in densely-forested high-relief mountains of central Japan. Our new 0.5-m DEMs from an unprecedentedly high-resolution LiDAR survey along the Neodani Fault now reveal a number of previously unknown fault scarps as well as other hidden geomorphic features. The survey achieves a ground-return density of 6.2 $m^{-2}$ out of a total shot density of as much as ~12.7 $m^{-2}$. The main factor to gain sufficient ground returns in unfavorable conditions is a large side lap of ~70% between flight swaths, which means that any specific area in the target zone is scanned three or more times from different angles. Evaluation of DEMs with resolution from 0.25 to 10 m assures that a 0.5m resolution LiDAR DEM is necessary for the detection of subtle tectonic breaks. Another key factor for complete detection of small tectonic–geomorphic features is the application of a recently developed DEM visualization "Red Relief Image Map (RRIM)", which allows mapping of all the small features with various sizes, orientations and morphology, overcoming major drawbacks of classic DEM visualizations. A very high-resolution LiDAR survey aided with RRIM visualization as used in this study provides a more reliable approach for the detailed mapping of slight active fault traces hidden under dense vegetation.

© 2012 Elsevier B.V. All rights reserved.

## 1. Introduction

Identification of faulted landforms provides the very basis for mapping active faults, or future sources of large earthquakes. Prominent faulted landforms, such as a large fault scarp cutting all the way through an open terrace surface or a series of offset streams that align on a clear geomorphic lineament, are robust visible evidence of repeated surface faulting associated with large earthquakes. However, recognition of subtle tectonic geomorphic features such as small fault scarps of less than a few meters high and small offset gullies of similar scale are also important because those small features record the most recent episodes of repeated faulting. Detailed information on recent fault activity usually cannot be captured by examining large-scale geomorphic features but is critical in assessing imminence of the next earthquake.

Recognition of small tectonic geomorphic features also has a clear impact in estimating the size of the future earthquake. Fault length is a primary parameter used for the size estimation, and thus discovery of small tectonic features on the extension of a mapped fault directly leads to a need to assume occurrence of a larger earthquake from the fault. More importantly, if small tectonic features are discovered between adjacent faults (or fault segments), rupture on one fault is more likely to propagate onto the other, resulting in a much larger "multi-fault" earthquake. Small tectonic geomorphic features hold keys to interpret or evaluate a whole fault system and are much more important than their size implies.

Despite the importance of small tectonic geomorphic features for evaluating the timing and size of future earthquakes, their identification is often hindered by vegetation. Classic aerial-photograph examination cannot detect small geomorphic features hidden under forest canopies, even with the trained eyes. This situation poses a big problem for a reliable seismic hazard assessment of mountainous and/or forested regions worldwide, in particular where regional strain is accommodated by complicated active structures. Though usually remote from population centers, these regions can still pose a great risk, as exemplified by recent destructive earthquakes, such as the 2005 Kashmir earthquake in Pakistan and the 2008 Wenchuan earthquake in China.

In recent decades, airborne LiDAR (light detection and ranging) surveying has been deployed to detect fine-scale tectonic–geomorphic features (e.g., Haugerud et al., 2003; Nelson et al., 2003; Sherrod et al., 2004; Bevis et al., 2005; Cunningham et al., 2006; Kondo et al., 2008; Arrowsmith and Zielke, 2009; Hilley et al., 2010; Zielke et al., 2010;

* Corresponding author. Tel.: +81 43 290 2799.
*E-mail address:* kaneda@faculty.chiba-u.jp (H. Kaneda).

0169-555X/$ – see front matter © 2012 Elsevier B.V. All rights reserved.
http://dx.doi.org/10.1016/j.geomorph.2012.11.001

Oskin et al., 2012), and to quantitatively explore characteristics of tectonic geomorphology (e.g., Hilley and Arrowsmith, 2008; Wechsler et al., 2009; Hilley et al., 2010; Zielke et al., 2010). One of the most attractive benefits of airborne LiDAR is its ability to see through the "bare earth" under vegetation because the ground emits a laser pulse that can be separated from canopy returns through filtering processes. In the U.S. Pacific NW and Europe, studies have successfully delineated earthquake surface ruptures under vegetation using 2-m LiDAR DEMs (digital elevation models) (Harding and Berghoff, 2000; Haugerud et al., 2003; Sherrod et al., 2004; Cunningham et al., 2006). However, recent LiDAR studies on the northern San Andreas Fault and central Japanese mountains also reported that some small tectonic breaks could not be identified with this resolution (Zachariasen, 2008; Lin et al., 2009; National Institute of Advanced Industrial Science and Technology, AIST, 2009). Especially in the case of high-relief Japanese mountains, we failed to find any youthful tectonic features by the 2-m DEMs from standard LiDAR surveys (National Institute of Advanced Industrial Science and Technology, AIST, 2009). Dense vegetation and topographic complexity likely increased the number of off-terrain laser hits, thereby reducing the number of ground laser strikes. The results showed that the ground data with low density failed to capture subtle geomorphic features. There is an urgent need to examine and expand the capabilities of LiDAR DEMs on their topographic expression.

One simple approach to address this issue is to increase spatial resolution of LiDAR ground return data. The development of recent LiDAR technique allows higher pulse-shot frequency. Lower flight altitude and more dense flight passes also aid more LiDAR pulses to transfer through the canopy and to reach the ground. Based on the enough data density, much finer resolution of LiDAR DEMs of tens of centimeters now can be constructed.

Another important, but often overlooked approach for more complete small-feature detection is to improve visualization of DEMs. High-resolution LiDAR DEMs are generally examined on a shaded relief map and/or a slope map. The former is widely used because it resembles what we see in the real world, but has a big disadvantage in that the appearance and impression of the image completely change depending on the direction of incident illumination. The latter is illumination-independent, but is quite different from our vision and cannot distinguish convexity and concavity. Fine-scale tectonic features with varying orientations will be obscured as a result of the limitations.

The purpose of this study is to explore effective LiDAR surveys and DEM visualization methods for mapping small tectonic geomorphic features in densely vegetated high-relief mountains. The study area is the northern part of the Neodani Fault, an active strike–slip fault in central Japanese mountains, where previous 2-m DEMs from standard LiDAR survey failed to detect small geomorphic features (National Institute of Advanced Industrial Science and Technology, AIST, 2009). We conducted an unprecedentedly high-resolution LiDAR survey in the same area, and the new LiDAR DEMs were compared with the existing 2-m LiDAR DEMs as well as topographic-map-based 10-m DEMs to examine if there was increased topographic expression of subtle features. In order to further enhance detectability of subtle topographic features, we applied a recently developed elaborate visualization "Red Relief Image Map (RRIM)" (Chiba et al., 2008) to the new LiDAR DEMs. Application of RRIMs to the high-resolution LiDAR DEMs allows fine expression of topography without shading, and serves as a very effective way for the detailed depiction of the slight tectonic–geomorphic features beneath dense vegetation. Though largely based on qualitative analyses, we suggest that a combination of a high-resolution LiDAR survey and RRIM visualization is effective for a complete and detailed mapping of slight active fault traces in densely vegetated high-relief mountains.

## 2. Study area

The Neodani Fault is an NW–SE striking active left-lateral fault in central Japanese mountains. It is one of the main faults that ruptured in the devastating 1891 $M_w$ 7.5 Nobi earthquake (Fig. 1; Matsuda, 1974). As multiple faults were involved in the 1891 earthquake, past behavioral patterns of those faults has received particular interest (e.g., Okada and Matsuda, 1992; Awata et al., 1999; Yoshioka et al., 2002; Kaneda and Okada, 2008). However, because of dense forest covers and rugged topography, the location of the northernmost part of the Neodani Fault has not yet been well defined by aerial photograph interpretation or by field investigation. In this study, we selected the northern part of the Neodani Fault as a target area of the new airborne LiDAR survey (Fig. 1). The area has the steepest topography along the fault zone, with altitudes of 156.2 to 1540.9 m, and average slope angle around 35°. The main rock type is Paleozoic–Mesozoic sedimentary rocks with penetration of Miocene granite. Most hillslopes are thickly covered by deciduous broad-leaved trees (mainly Japanese oaks and beeches), evergreen coniferous trees (mainly Japanese cedars and cypresses), undergrowth of bamboo grasses (Kumazawa) and other thorny bushes. The climate of the study area is warm and temperate with a mean annual temperature of ca. 8–16 °C. The average annual precipitation is about 2500 mm (Japan Meteorological Agency, 1971).

## 3. Data and methods

### 3.1. Very high-resolution LiDAR survey

A very high-resolution airborne LiDAR survey was conducted along the northern part of the Neodani Fault (Fig. 1) during the leaf-off season of January 2008. The target area is ~16 km long and ~1.25 km wide. A Cessna 208 with a Leica ALS 50 LiDAR instrument was flown at an altitude of ~1250 m, which is a lower limit in high-relief mountain areas, scanning the topography with a pulse-shot frequency of 50–60 kHz, scan angle of ±~10°, and a swath width of ~430 m. The LiDAR survey was carried out by Kokusai Kogyo Co., Ltd., Japan.

The key factor for the achievement of a very high shot density along the fault is an exceptionally large number of flight passes in the target zone. We set up as many as 13 passes targeting the 1.25-km-wide zone, as compared to five passes targeting the zone of similar width in the recent LiDAR survey project ("B4 project") along the southern San Andreas Fault (e.g., Arrowsmith and Zielke, 2009; Zielke et al., 2010). This is equivalent to a side lap (overlap of swaths) of ~70%, which means that any specific area in the target zone is scanned three or more times from different angles. This sampling approach is more efficient than simply increasing the pulse shot frequency or decreasing flight height and proved particular useful for gaining higher-density ground returns in steep topography. The resultant average shot density of the laser points before filtering is as much as ~12.7 $m^{-2}$, ranging from 6.7 to 24.6 $m^{-2}$. This not only overwhelms that of the previous 2003–2004 LiDAR survey (~1.2 $m^{-2}$) that will be described later, but is even much higher than that of the more recent B4 project along the San Andreas (~3.6 $m^{-2}$; Arrowsmith and Zielke, 2009). The acquired elevation data has a horizontal accuracy of 0.320 m, a vertical accuracy of 0.085 m, and an absolute RMS accuracy better than 0.15 m.

Automatic filtering was performed to eliminate vegetation and man-made structures using an adaptive filter that evaluates changes in slopes and elevation along the scan line. The filtering is based on the assumption that natural terrain variations are gradual, rather than abrupt. In contrast, the boundary between ground and non-ground points should exhibit an abrupt change in elevation and slope. The joint use of slopes, elevation differences, and local elevations can help to filter non-ground points more accurately. In addition, we closely checked the automatic filtering data and manually eliminated or restored the error points to construct more realistic ground return data. After the filtering, the average shot density of ground points is still around 6.2 $m^{-2}$, indicating one out of two shots reached the ground on average. Based on the ground point data, 0.5-m DEMs were generated. Higher resolution DEMs (0.25 m) were also generated for portions of the fault where average shot density is larger than 12.0 $m^{-2}$.

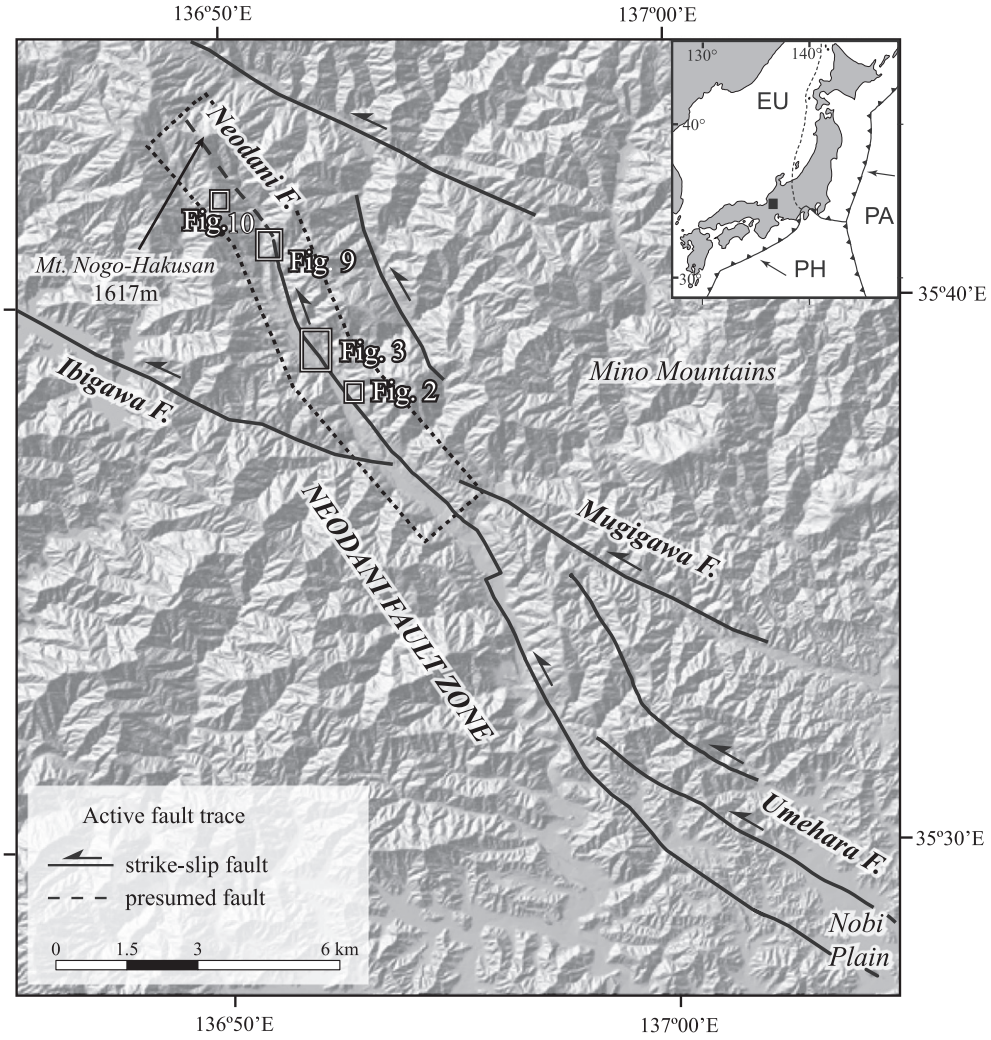


**Fig. 1.** Topography and locations of the Neodani Fault. Area of the 2008 LiDAR survey is shown as dotted box. Half-sided arrows indicate the sense of slip along strike–slip faults. The shaded topographic relief is based on 10-m digital elevation models (DEMs) of the Geospatial Information Authority of Japan. Abbreviations in the inset: EU — Eurasian Plate; PA — Pacific Plate; and PH — Philippine Sea Plate.

### *3.2. Preexisting digital topographic data and comparison of various-resolution DEMs*

An airborne LiDAR survey was carried out for the entire Gifu Prefecture in 2003 and 2004 where the Neodani Fault is located. The purpose was to develop new-generation large-scale base topographic maps for development, management, and natural-hazard assessment. The standard-specification LiDAR survey with a flight height of ~2000 m above ground and a pulse-shot frequency of ~15 kHz resulted in an average shot density of ~1.2 $m^{-2}$ along the Neodani Fault. This is comparable with contemporary LiDAR surveys in the NW United States (Haugerud et al., 2003; ~1 $m^{-2}$) and Europe (Cunningham et al., 2006; ~1.6 $m^{-2}$), both of them successfully delineated geomorphic features hidden under forest canopies.

However, 2-m DEMs derived from the 2003–2004 survey could not capture the known small tectonic features in the forested mountains (Lin et al., 2009; National Institute of Advanced Industrial Science and Technology, AIST, 2009). These 2-m DEMs were constructed only with automatic filtering because they were not intended to detect small geomorphic features. The inadequate filtering process and dense vegetation likely resulted in the poor detection of small features. We thus reprocessed the original point-cloud data to produce new bare-earth 2-m DEMs through automatic and manual filtering (the same procedure done for the 2008 higher-resolution LiDAR data). To distinguish the two sets of DEMs, we designate the original 2-m DEM as 2-m DEM (A), and the reprocessed 2-m DEM as 2-m DEM (M) in the following text.

In addition to the preexisting LiDAR data, we also prepared a topographic-map-based 10-m DEM for comparison. This was constructed from 10-m contours of 1:25,000 topographic maps of the Geospatial Information Authority of Japan (formerly Geographical Survey Institute) by Hokkaido-Chizu Co. Ltd., which had been the highest-resolution DEM before the advent of airborne LiDAR.

The Nogo area on the northern part of the Neodani Fault was selected as a test site to assess how high-resolution DEMs are needed to map fine-scale tectonic–geomorphic features in densely forested mountains (Figs. 1 and 3). The NNW–SSE trending fault traces contain various types and scales of tectonic features under dense forest, including shutter ridges, deflected gullies and uphill-facing scarps. The ability to express fine-scale topographic features at various resolutions of DEMs from 10 m, 2 m (A), 2 m (M), 0.5 m to 0.25 m were compared using shaded relief maps. The average shot density of ground points of the area is high enough for the construction of the 0.5-m and 0.25-m DEMs.

### *3.3. DEM visualization*

To visualize the aforementioned DEMs, we produced commonly-used geomorphic images, including a shaded relief map, a slope map, as well

as a slope map overlaid on a tinted elevation map. In addition, we applied the "Red Relief Image Map (RRIM)" (Chiba et al., 2007, 2008) to the DEMs, which is a multi-layered illumination-free image that can visualize the topographic slope, concavities and convexities simultaneously.

RRIMs are based on image overlay of two topographic elements: slope angle and the new parameter $I$ (Chiba et al., 2007, 2008), which is defined as a combination of positive openness $O_p$ and negative openness $O_n$:

$$I = \left(O_p - O_n\right)/2$$

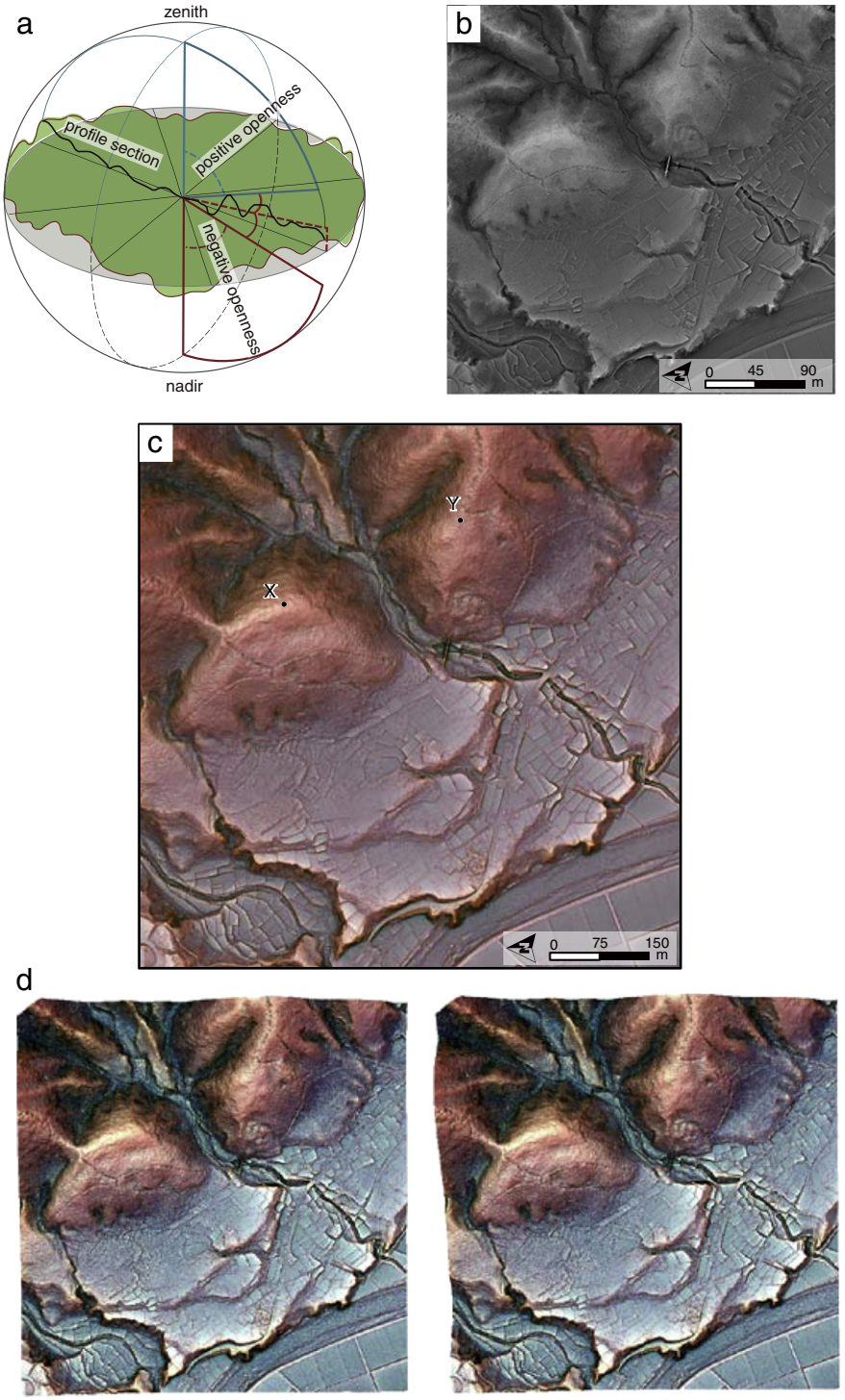


**Fig. 2.** Concept and example of the Red Relief Image Map (RRIM). (a) Concept figures of positive openness, negative openness and a negative $I$ value. Positive openness is average of eight zenith angles of a surface spot along compass directions within radial limit, while negative openness is average of the eight nadir angles. Zenith angle is the largest angle between the surface spot and the topographic profile points, while nadir angle is the smallest angle. $I$ value is difference between positive openness and negative openness divided by 2. (b) An example of the $I$ value map. (c) An example of the RRIM. See Fig. 1 for locations of (b) and (c).

where $O_p$ and $O_n$ respectively represent surface concavities and convexities observed from a given zenith (Fig. 2a; Yokoyama et al., 1999, 2002). The parameter *I* describes concavities as positive values, and convexities as negative values, which is not only very sensitive to local topographic change, but also can distinguish concavities from convexities in a single image. Fig. 2b is an example of the *I*-value map. Higher *I* is expressed in a brighter gray, and lower *I* is represented by a darker gray. It resembles a shaded-relief image but is independent of the direction of incident light. An RRIM is then generated by an overlay of a red-colored slope map on the *I*-value map (Fig. 2c). It accentuates the three-dimensional topography on a single image, where the *I*-value virtually performs an illumination role, and saturation of red color describing the steepness of topography. The reason for the use of red color to describe slope angle is that it empirically proved to have the richest tone for human eyes, although other colors can also be applied (Chiba et al., 2007).

In addition to illumination-independent 3D visualization, RRIMs are sensitive to subtle topographic changes. RRIMs can be tuned to express various scales of topography in detail by adjusting the zenith position (Fig. 2a). These advantages would maximize small-feature detectability of high-resolution LiDAR DEMs.

A disadvantage of RRIMs is that they cannot compare heights of distant places, such as ridge crests across a valley (points X and Y in Fig. 2c, for instance), because RRIMs by definition take account of slope (first derivative of height) and parameter *I* (comparable to second derivative of height) and do not contain height information. To overcome this disadvantage, we further produce stereo-paired RRIMs using perspective

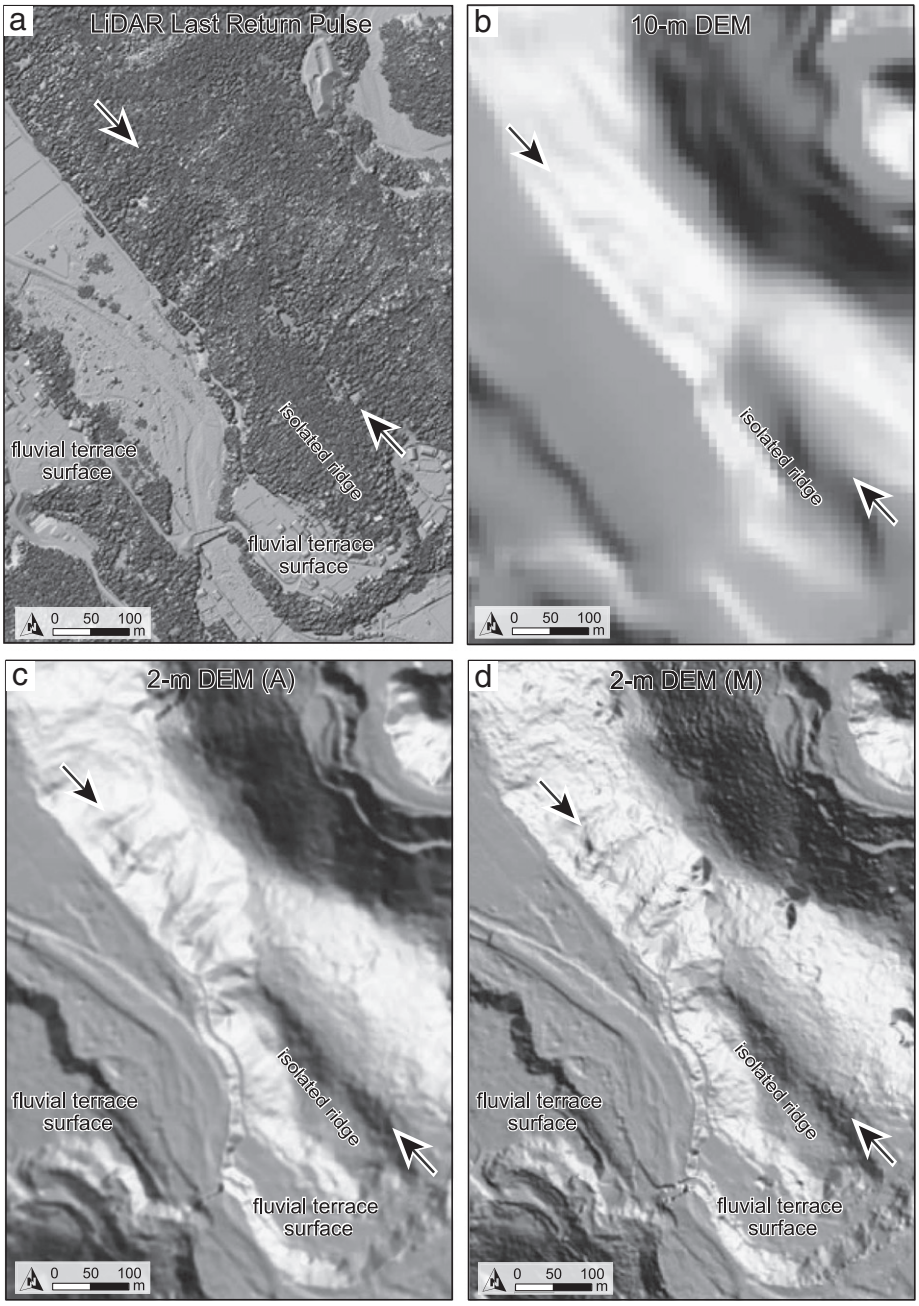


**Fig. 3.** Shaded relief maps from DEMs of various resolutions for the Nogo area. The illumination direction is set from the southwest, perpendicular to the fault trend to emphasize fault topography. See Fig. 1 for the location. (a) 0.5-m LiDAR DEM without filtering vegetation. (b) 10-m DEM. (c) 2-m DEM only with automatic filtering. (d) 2-m DEM with both automatic and manual filtering. (e) The 0.5-m DEM. (f) The 0.25-m DEM.

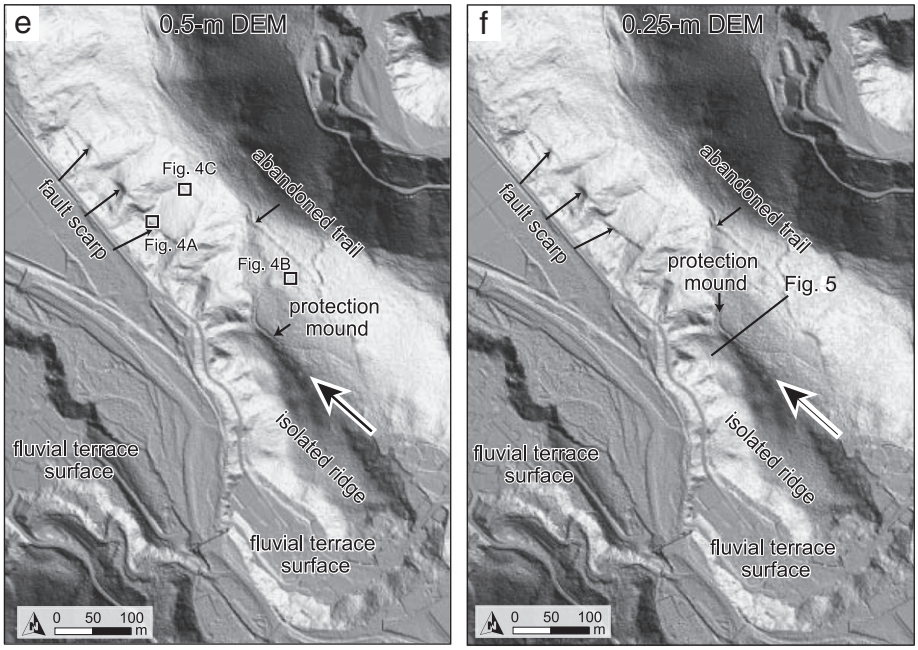


**Fig. 3** (*continued*).

images taken from nearly perpendicular but slightly different angles on the basis of the LiDAR DEM (Fig. 2d). The stereo view allows an excellent 3D geomorphic expression, impressively representing the subtle topography in extraordinary details and great reality. Stereo-paired RRIMs are an ideal topographic visualization that contains all of the three basic morphometric parameters, height and its first and second derivatives, which has not been realized by any preexisting DEM 3D visualizations including stereo images based on shaded relief maps or slope maps, and anaglyph 3D images (stereoscopic images using red and blue colors; the base image is usually a shaded relief map). While a single RRIM is easier to handle and has enough quality and information for just picking up small geomorphic features, stereo-paired RRIMs serve as a powerful tool to understand their geomorphic contexts and interpret their origins.

## 4. Results

### *4.1. Topographic expression ability of various-resolution DEMs*

Shaded relief maps are generated from the 10-m to 0.25-m resolution DEMs (Fig. 3). The illumination direction of the shaded relief maps is set from the southwest, roughly perpendicular to the general fault strike to emphasize the fault topography. The coarsest 10-m DEM map depicts the general topographic arrangement such as the NW–SE trending main mountain ridge and the terrace surface in the southwest (Fig. 3b), but it is difficult to detect any active fault traces from this image. The 2-m DEM (A) describes the shape of the isolated ridge in detail but no other fault features can be detected from it (Fig. 3c). The 2-m DEM (M) expresses topography more sharply, where even something like a small scarp appears (Fig. 3d). The difference in the visual quality reflects the smoothing process of automatic filtering for the production of the 2-m DEM (A).

The 0.5-m DEM derived from our very high-resolution LiDAR survey intricately portrays various small geomorphic features in the northwest (Fig. 3e), a part of which were not found previously. The prominent NW-trending uphill-facing scarps are interpreted to be fault scarps as they are exactly on the trace of the Neodani Fault. Other small-scale features visible on this image are mostly artificial landforms confirmed by our field work and examination of historical documentation. Artificial features included an abandoned small trail and protection mound that had been used as recently as 150 years ago, and abandoned waterway for hydroelectricity that was in operation ~90 years ago. Field photographs show one of the small fault scarps ~2 m high (Fig. 4a), and an abandoned protection mound ~1 m high (Fig. 4b). A part of the mound less than 20 cm high cannot be found even in the Fig. 3e. The shaded relief of the 0.25-m DEM, the finest image in this study, appears a little sharper than that of the 0.5-m DEM, although no additional topographic features can be detected (Fig. 3f).

These results indicate that, 0.25 to 0.5 m resolutions of the LiDAR DEMs are probably the desired resolution to detect subtle tectonic–geomorphic features. To examine this inference, a field total-station survey was carried out across the trough northeast of the isolated ridge, and topographic profiles from the survey and the different DEMs were compared (Fig. 5). As the survey site is in a deep forest far from bench marks, only relative positions and heights were measured, but later, the absolute horizontal position of the profile was able to be precisely determined using artificial and natural features that are recognized in both the field and LiDAR images. The profile extracted from the 10-m DEMs barely shows the presence of the trough, and its depth and shape are quite different from actual topography. The profile of the 2-m DEM (A) excellently represents the depth and shape of the trough, but the somewhat smoothed profile does not allow identification of the subtle topographic breaks, while that of the 2-m DEM (M) detects one of topographic breaks of the protection mounds (A of Fig. 5). Both of the profiles extracted from the 0.5-m and 0.25-m DEMs match the field-surveyed actual topography well, delineating all of the slight topographic breaks.

To quantitatively evaluate the quality of these DEMs, we calculate height errors of the profiles based on the criterion data from the total station survey. We prepared the 0.25-m interval "actual profile" by interpolation of the total-station data, on the basis of which the minimum RMS errors of each DEM profiles are searched by moving the profile vertically (Fig. 6). The error of the 10-m DEM is by far largest (2.67 m) as is expected from the profile's appearance, whereas those of the 2-m DEMs show a marked improvement down to a value of 0.518–0.558 m. The 0.5-m DEM further improves the profile quality (0.456 m), but the quality becomes slightly worse when we go to the finer resolution of the

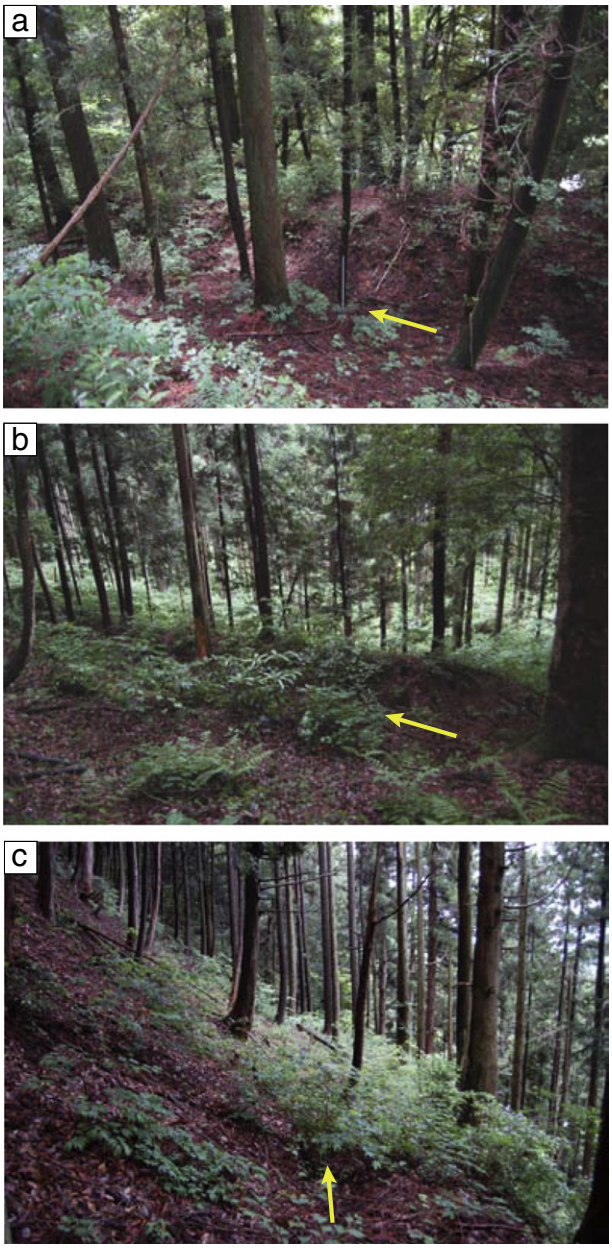


**Fig. 4.** Field photographs of fine-scale topographic features. (a) Small scarp 0.5 m high detected by the 0.5-m LiDAR DEM. (b) Abandoned man-made protection mound detected by the 0.5-m LiDAR DEM. A part of which at height lower than 20 cm cannot be detected. (c) Small step ~70 m northeast of the small scarp of (a). Note that there is no trough along this feature.

0.25-m DEM in terms of a value of RMS error (0.490 m). The reason is unclear, but one possible explanation is that minor facets in the 0.25-m DEM, resulted from a lack of consistently dense points, may have produced larger errors. In any case, our analysis shows that there is no additional quality refinement from the 0.5-m to 0.25-m DEMs.

### 4.2. Comparison of RRIM with other geomorphic visualization methods

To find an effective visualization method for the detection of the small tectonic–geomorphic features, we utilized the 0.5-m DEM to create an RRIM, and compared it with common geomorphic visualization maps, including a shaded relief map, a slope map, and a slope map overlaid on a tinted elevation map (Fig. 7).

The shaded relief map for the same area as in Fig. 3 is shown with different illumination directions, i.e., from northwest, roughly parallel to the general fault trend (Fig. 7a). It reveals significantly different expression of topography from that of Fig. 3e: the prominent NW-trending uphill-facing fault scarps now almost disappear, while SE-facing head scarps and valley slopes become predominant components of the image. We may be able to tune an illumination angle to produce a shaded relief image which can better visualize the above features, but the image would in turn miss other features that are visible in Figs. 3e and 7a. Comparison of Figs. 3e and 7a clearly demonstrates a need to examine many kinds of shaded-relief maps for the same area to pick up all the features that are latently expressed in the DEM.

The slope map (Fig. 7b) is an excellent visualization representing all the features that are expressed in Figs. 3e and 7a, including fault scarps, head scarps, and valley slopes. However, it cannot distinguish if a spot is higher or lower than a surrounding area because this map does not include height information. Moreover, with the slope map alone, one cannot discriminate concavity from convexity. For example, a ridge at the northeast corner of the image (circled in Fig. 7b) may look like a depression.

Elevation information is overlaid to the slope map to overcome this drawback (Fig. 7c). In the figure, slope performs an illumination role and color phase describes the height of topography. The ridge in the northeast corner is now recognized as a protruding object, while other sections of the image remain unclear, sunk beneath the darker elevation colors. As long as height information is expressed with ramped color, areas with the highest and/or lowest elevations are inevitably masked with dark tone. This effect is weakened if we use lighter colors, but these colors cannot create high color gradient, resulting in weaker height information as well.

The RRIM for the same area (Fig. 7d) not only delineates all the fine-scale geomorphic features more complexly, but explicitly expresses convexity and concavity in a single image without shadow. It resembles the slope map or the map overlaid by slope and elevation, but its sharpness and three-dimensional appearance are far superior (Figs. 7 and 8). As for the ridge at the northeast corner, the RRIM now clearly shows its convex topography. It overcomes the weak points of the above topographic visualization methods. When the RRIM is remade into a stereo-pair (Fig. 7e), the overall topographic relief becomes much clearer, and surmounts the disadvantage of RRIMs — incapability to compare heights of distant places.

The RRIM increases the expression of the fine topographic features in the study area, especially for the slight topographic edge and concavo-convex shape. For example, the image clearly delineates the edge of the subtle landslide in the northwest corner where no fault trace appears, indicating that the landslide occurred after the last faulting activity. In addition, the slope map (Fig. 8a) can represent two NW-trending subparallel features indicated by arrows, but the image cannot determine if the topography is just a step without concavity or a linear trough accompanied by an uphill-facing scarp. The RRIM (Fig. 8b) clearly reveals that the upper (northeastern) feature is a step (Fig. 4c), and the lower (southwestern) feature is an uphill-facing scarp (Fig. 4a), which is verified by our field check (Fig. 4c and a, respectively) and the RRIM stereo view (Fig. 7e).

We are sure that experienced users are able to recognize the above features by closely examining and comparing Figs. 3e and 7a, b, but our point is that RRIMs allow the same level of interpretation with a single image, exempting from making and examining many kinds of images from DEMs. The effect of RRIMs would be much greater when we intend to map a vast area, although good-quality LiDAR DEMs are a prerequisite.

### 4.3. Detection of subtle geomorphologic features in densely forested mountains

According to the above results, the RRIM of the Neodani Fault zone was therefore created based on the 0.5-m LiDAR DEM to detect

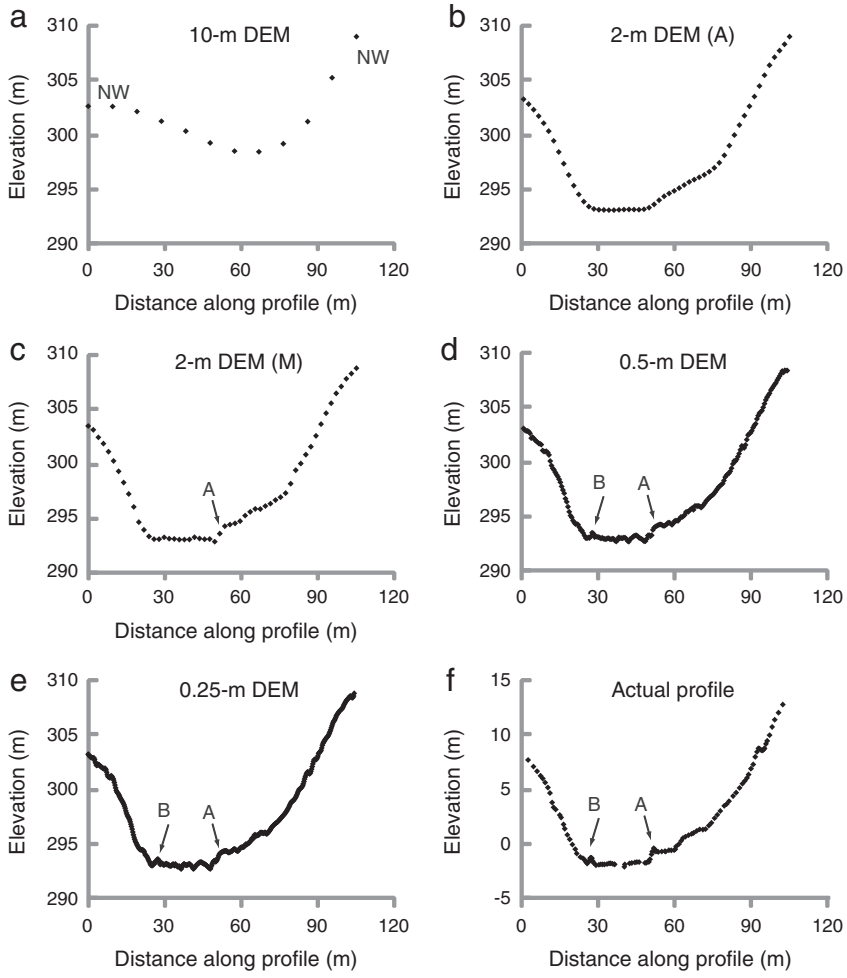


**Fig. 5.** Topographic profiles from the DEMs of various resolutions. See Fig. 3f for location. (a) 10-m DEM. (b) 2-m DEM only with automatic filtering. (c) 2-m DEM with both automatic and manual filtering. (d) 0.5-m DEM. (e) 0.25-m DEM. (f) Profile surveyed using a total station. Note that the vertical axis of the profile only shows a relative elevation because the surveyed site is in the deep forest far from bench marks.

geomorphic features hidden by the dense vegetation cover. A number of interesting features were newly revealed in the RRIM, which have never been found by 1:10,000-scale aerial photograph interpretations, previous field investigations, and the pre-existing 2-m LiDAR DEMs. The followings are two examples of the effective mapping of small-geomorphic features using the 0.5-m LiDAR RRIM.

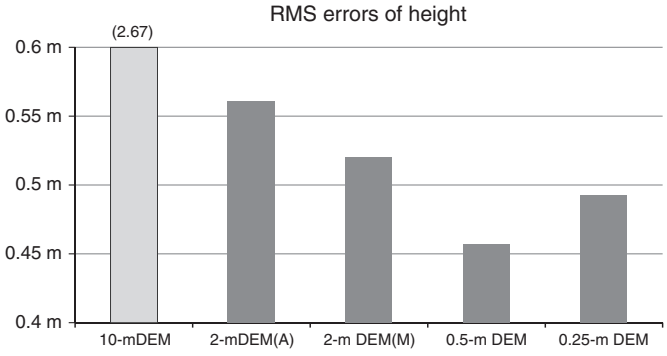


**Fig. 6.** Minimum RMS errors of height for a topographic profile extracted from the 0.25–10 m DEMs, compared to data measured by a field total-station survey. Light gray column shows a markedly large RMS error of 2.67, out of the range of the Y axis.

*4.3.1. Systemically deflected channels along the Neodani Fault near Nogo Valley*

In the north-central part of the study area, the Neodani Fault passes through steep, west-facing hillslopes on the left bank of the Nogo River. The area is difficult to access because of no available trails, dense forest, thick thorny bush, and steep slope angles about 40°. The RRIM reveals a series of sinistrally deflected channels dissecting the steep hillslope, between which uphill-facing scarps extend along NNW-trending fault (Fig. 9). Although the sinistrally deflected valleys and ridges can be barely detected from available 1:10,000 aerial photographs, the uphill-facing scarps 1–6 m high could not be identified because of thick vegetation. These scarps have been trapping sediments after their formation and thus serve as a potential site for small trenching to reveal timing of recent faulting events. A channel cut off is visible in the RRIM, which is difficult to be identified even in the field because the steep hillslope and dense bush cover prevent a complete observation of this feature (Fig. 9, inset).

In addition, we found that the RRIM is excellent for locating ourselves in the field, where forest canopies hamper the utility of portable GPS devices, because it congregates all the small and large topographic features in a single image. In the field investigation, we

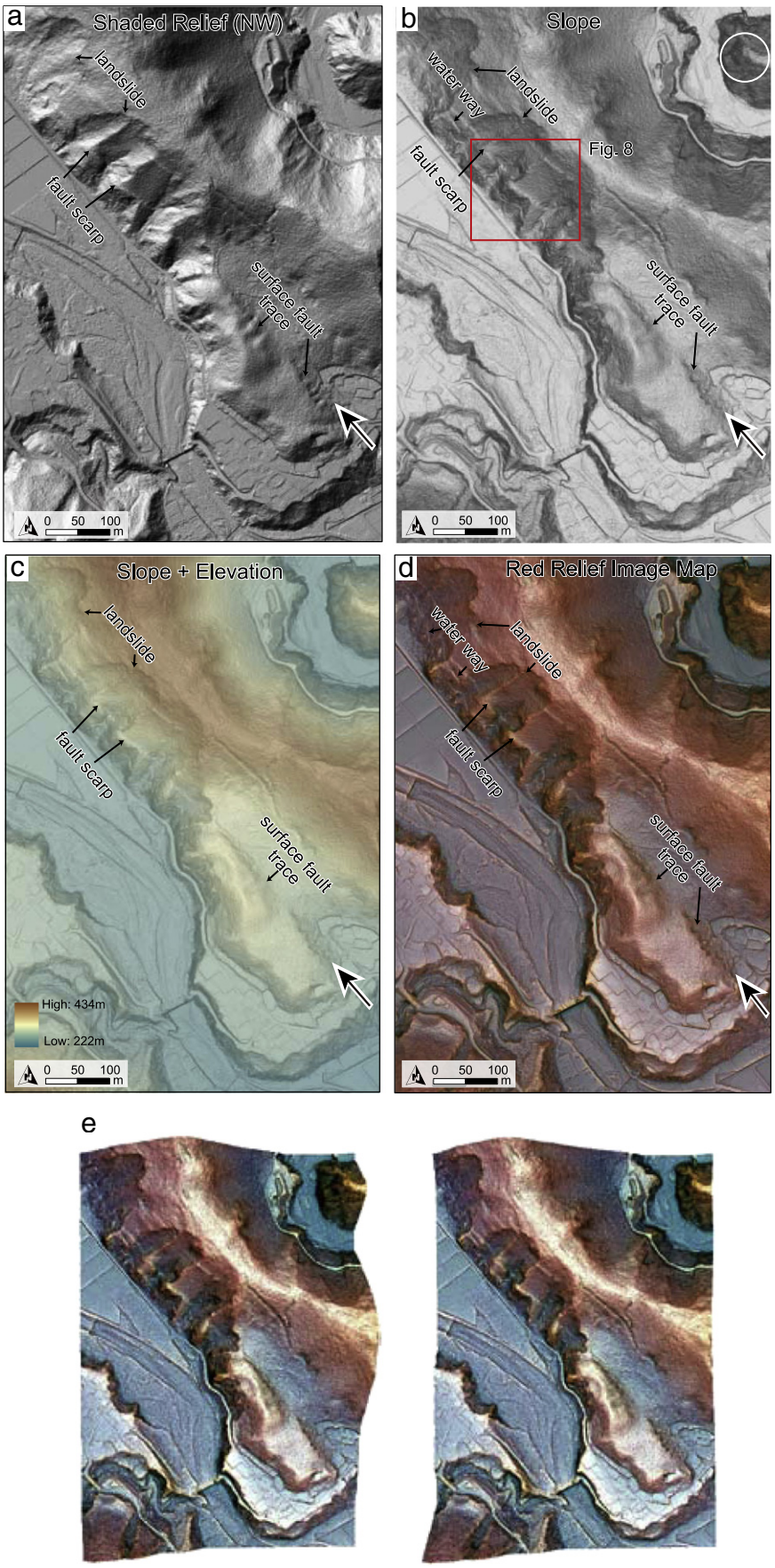


**Fig. 7.** Various geomorphic visualization maps for the Nogo area. See Fig. 1 for location. (a) Shaded relief map with illumination direction from northwest. (b) Slope map. (c) Overlay of elevation with slope. (d) Red Relief Image Map (RRIM). (e) Stereo-paired RRIMs.

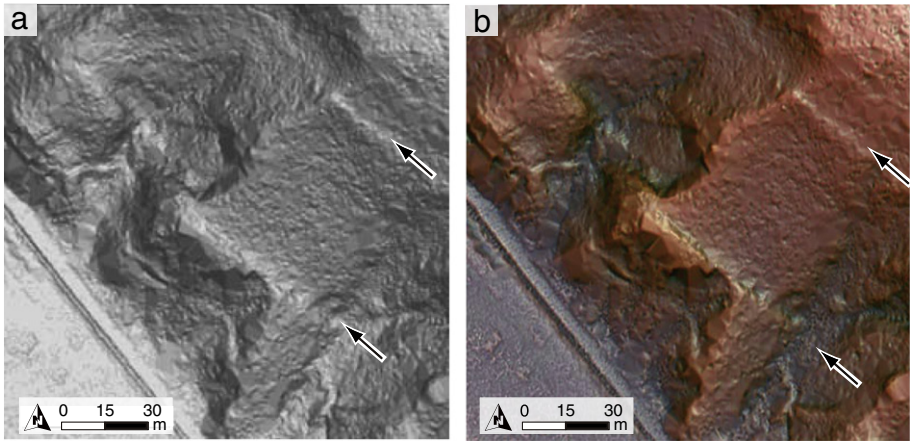


**Fig. 8.** Enlarged view for a part of the Nogo area. See Fig. 7b for location. (a) Slope map: two linear topographic breaks run parallel across a southwest-facing slope as indicated by arrows. It is unclear if the break is a step without concave or an uphill-facing fault scarp accompanying a linear trough. (b) RRIM. This image clearly demonstrates that the upper (northeastern) break is a step, whereas the lower (southwestern) break is an uphill-facing fault scarp.

confirmed the above-mentioned detected geomorphic features and found several fresh fracture zones in the bedrock along the deflected channels.

*4.3.2. Numerous sagging features around the northernmost Neodani Fault*

Further to the north, where higher mountains are more rugged and the location of the Neodani Fault has not been well defined, the RRIM

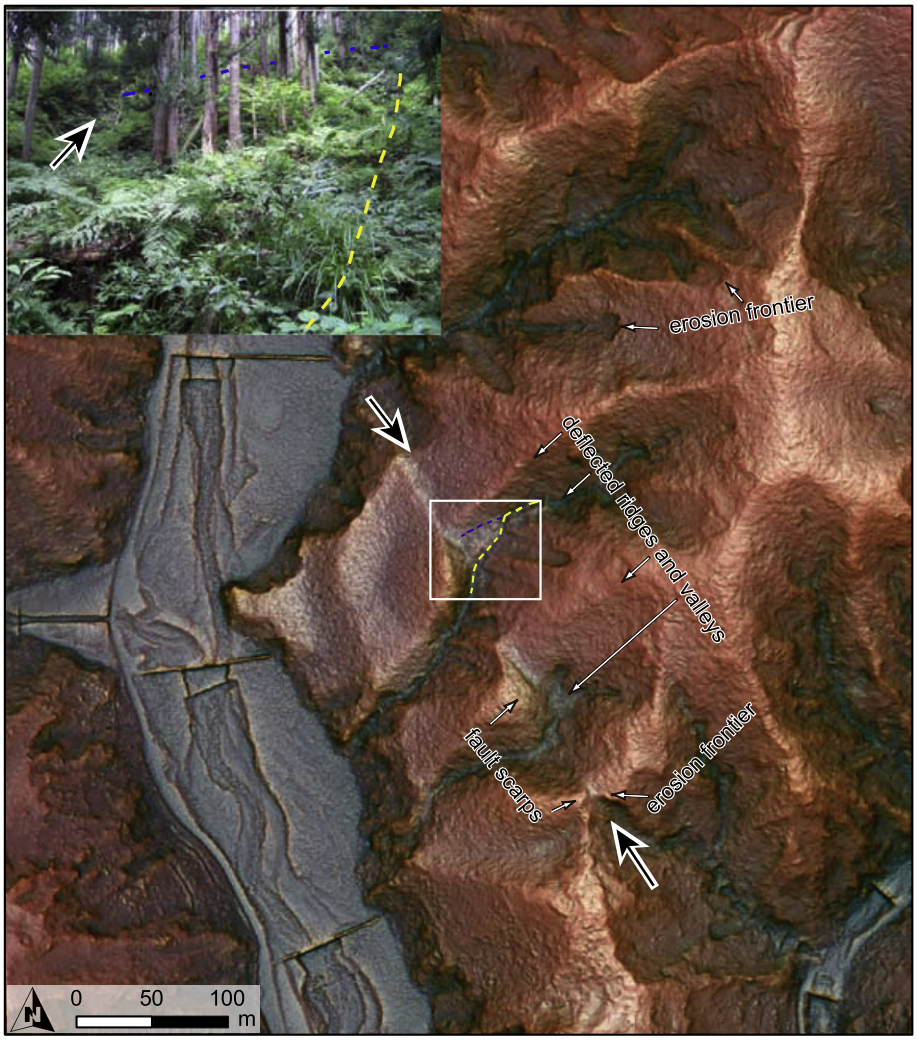


**Fig. 9.** Systemically deflected channels near Nogo Valley, the northern Neodani Fault, as evident from the 0.5 m LiDAR RRIM. Inset is a field photo, where a shortcut of a small channel is visible in the RRIM, but is difficult to recognize even in the field because of steepness and dense bush. White line box: location of the photo. Blue dashed line: original channel position. Yellow dashed line: present channel after short cut.

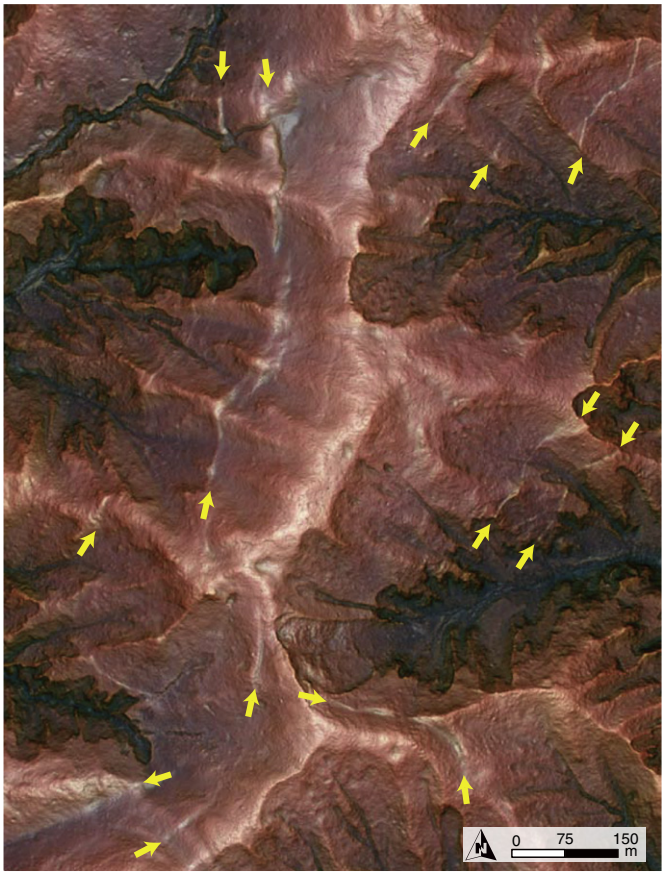


**Fig. 10.** Numerous small geomorphic features similar to tectonic features around the northernmost Neodani Fault. Although their trends (indicated by yellow arrows) and distribution suggest that they are principally gravitational in origin, or sagging features, apparent concentration of these features around the northernmost Neodani Fault implies their possible link to fault activity.

reveals interesting geomorphic features around the Neodani Fault. Unfortunately, the fault trace is still not well constrained even with the RRIM, although we found very small fragments of a probable fault scarp at a few localities in the area, most likely because rapid erosion with mass-wasting activity have erased most of the tectonic features.

An unexpected discovery in the area is numerous small geomorphic features subparallel to major ridges (Fig. 10). Local morphology is very similar to tectonic features, i.e., uphill-facing scarps and linear troughs, but their trends and distribution suggest that they are principally gravitational in origin, or sagging features. However, apparent concentration of those features around the northernmost Neodani Fault implies possible link to the fault activity. Formation and growth of those newly-found features may be correlated to paleoearthquakes because enhanced ground shaking and concentrated static deformation around the fault tip might be a big trigger for gravitational deformation. Although detailed study is required to test this hypothesis, this example demonstrates the potential of high-resolution LiDAR RRIMs for geomorphological research in forested mountains.

## 5. Discussion

### *5.1. Necessary resolution of LiDAR data to detect subtle geomorphic features under vegetation cover*

The above-mentioned results showed that the LiDAR DEMs with resolution higher than 0.5 m revealed abundant and detailed geomorphic features under dense vegetation cover, which could not be detected in the other sets of DEMs with lower resolutions. Using the 0.5-m DEMs, the smallest detectable scarp under the vegetation cover should be ~20 cm in height because the man-made mound, which is similar in shape to a small scarp, was difficult to detect when the height was lower than 0.2 m (Fig. 4a). In places without vegetation cover, however, smaller topographic breaks in slope around 10-cm high were identified. Although previous studies used 2-m resolution DEMs from standard LiDAR surveys to delineate the geomorphic features of active faults under dense vegetation in the USA and Europe (e.g., Prentice et al., 2003; Sherrod et al., 2004; Cunningham et al., 2006), our results indicate that 2-m resolution is obviously insufficient for the current study site. In the case of the central Japanese mountains, a 0.5-m DEM derived from a very high-resolution LiDAR survey is required to delineate hidden geomorphic features. In particular, the flight plan that incorporates many flight passes and large side laps (~70%) have worked efficiently to achieve a sufficient number of ground returns even in Japanese mountains, where particular vegetation types such as evergreen trees and the underbush of bamboo grass and their high density significantly prevent laser pulses from reaching the ground.

One of the reasons why 0.25–0.5 m resolution data are required is that these resolutions are similar to, or finer than the features of interest: meter-scale earthquake offsets. However, even such high resolution data may be insufficient for some types of geomorphological research. For instance, when smaller-scale surficial asperities such as small rills or periglacial patterned grounds are of interest, finer-resolution DEMs should be required. On the contrary, coarser resolution data may be more cost and time efficient when we look at larger-scale geomorphology.

Theoretically the 0.25-m DEM should express geomorphic features better than the 0.5-m DEMs. However, our quantitative analysis shows no significant difference between them, although the image from the 0.25-m DEM looks slightly sharper than that from the 0.5-m DEM. This is probably due to the size of the laser pulse arriving on the ground (i.e., "footprint"). Given our flight height of ~1250 m and beam angle of 0.33 mrad, the nominal footprint size is ~0.41 m, which is larger than 0.25 m. The 0.25-m DEM provides topographic information similar to that from the 0.5-m DEM, while its file size is larger by a factor of 4.

Our results also indicate that the size of the laser pulse and the poor laser-pulse penetration through vegetation are essential snags of the LiDAR technique. However, there is still ample scope to improve the LiDAR survey methods for forested mountain areas. One is decreasing the diameter of the laser pulse to improve the laser-pulse penetration and data quality. The simplest way is to set the flight height as low as possible, but this method leads to a narrower swath width, a smaller side lap, and lower ground-return density. However, new LiDAR equipments emit narrower laser pulses like 0.22 mrad, which realizes a foot-print diameter of ~20 cm from the height of 900 m. In addition, another way to overcome LiDAR snags is to improve filtering methods. We repeated revising errors by various types of data format such as point, TIN and contour, and checked errors using different visualization methods considering topographic characteristics. The effect of the trial is clear if the 2-m DEM (A) and 2-m DEM (M) are compared (Fig. 3c, d), and thus it is a possible and latent way to improve data quality to some extent.

### *5.2. Effectiveness of LiDAR RRIMs in mapping fault traces*

We applied the RRIM technique to the LiDAR DEMs to overcome the weakness of commonly used visualization methods. It revealed rich and diverse records of previously unknown geomorphic features under vegetation cover. RRIMs are good at detecting local topographic change and distinguishing concavity and convexity without shadow, and stereo-paired RRIMs further improve topographic expression of DEMs. The combination of a high-resolution LiDAR DEM with an RRIM thus enhances geomorphologists' ability to extract subtle topographic changes.

Because a high-resolution LiDAR RRIM delineates all topographic features in one image in detail, it may be the best replacement of field investigation for areas that are difficult to access. Because LiDAR RRIMs can finely express various types of topographic features, they are useful to examine the relations between tectonic faulting and other geomorphic processes such as erosion, mass-wasting and channel extension (e.g., Figs. 3, 8, 9 and 10). This would enhance our understanding of the formation and evolution of fault morphology.

Although RRIMs overcome most of the weak points of commonly used visualization methods, they are not always the best. For instance, a shaded-relief map with the best illumination direction can often emphasize the target feature more effectively than an RRIM (Figs. 3e and 7d). This means that we need to choose, tune, and combine various visualization methods depending on our purposes, although RRIMs can serve as a robust foundation to start with.

This study is largely qualitative and subjective, to look for the most powerful method to maximize the utility of LiDAR surveys and aid in researchers' eyes. The results show that the combination of LiDAR DEMs and RRIMs can greatly improve the detection ability of geomorphic–tectonic features. Such accurate mapping of active fault traces, including subtle tectonic features, will lead to more practical assessments of seismic hazard. Especially where a fault terminates to step to another fault, detection of subtle active fault traces in the step area holds key for evaluating potential rupture propagations across the step.

## 6. Conclusions

Our new 0.5-m DEMs from the unprecedentedly high-resolution LiDAR survey along the Neodani Fault reveals a number of fault scarps and other geomorphic features hidden under vegetation, which were not detected by the preexisting 2-m DEMs from a standard airborne LiDAR survey. The flight plan incorporated many flight passes and large side laps (~70%) in the target zone, and scanned any specific area in the zone more than three times from different angles, allowing the implement of the high-resolution survey. The result reveals that 0.5 m is the appropriate resolution to create DEMs from airborne LiDAR at present. The 0.25-m DEM has no significant improvement over the 0.5-m DEM in the expression of small-scale topography, as the size of the laser footprint (~0.41 m) probably hampered the improvement. It is further found that RRIMs and their stereo-paired use are effective DEM visualizations for mapping small tectonic–geomorphic features with various sizes, orientations and morphology, overcoming major drawbacks of classic visualizations. Very high-resolution LiDAR surveys aided with RRIM visualization provide a reliable approach for detailed geomorphological mapping.

## Acknowledgments

We are grateful to Angela Zhao, Freda Fu, Tadashi Maruyama, Takashi Azuma, and Toshikazu Yoshioka for useful discussion, suggestions and supports. Thoughtful comments by Takashi Oguchi and Thad Wasklewicz are very helpful for the improvement of the manuscript. This work was supported by the Japan Nuclear Energy Safety Organization (JNES). Zhou Lin was supported by the NSFC grant 41072165 and the FRF grant 2010QNA3034 during 2010–2012.

## References

Arrowsmith, J.R., Zielke, O., 2009. Tectonic geomorphology of the San Andreas Fault zone from high resolution topography: an example from the Cholame segment. Geomorphology 113, 70–81.

Awata, Y., Kariya, Y., Okumura, K., 1999. Segmentation of the surface ruptures associated with the 1891 Nobi earthquake, central Honshu, Japan, based on the paleoseismic investigations. Interim Report EQ/99/3, Geological Survey of Japan, Tsukuba (in Japanese, with English abstract).

Bevis, M., Hudnut, K., Sanchez, R., Toth, C., Grejner-Brzezinska, D., Kendrick, E., Caccamise, D., Raleigh, D., Zhou, H., Shan, S., Shindle, W., Yong, A., Harvey, J., Borsa, A., Ayoub, F., Elliot, B., Shrestha, R., Carter, B., Sartori, M., Phillips, D., Coloma, F., Stark, K., 2005. The B4 Project: scanning the San Andreas and San Jacinto Fault zones. Eos Transactions AGU 86 (52) Fall Meeting Supplement, Abstract H34B-01.

Chiba, T., Suzuki, Y., Hiramatsu, T., 2007. Digital terrain representation methods and Red Relief Image Map. Journal of the Japan Cartographic Association 45, 27–36 (in Japanese, with English abstract).

Chiba, T., Kaneda, S., Suzuki, Y., 2008. Red Relief Image Map: new visualization method for three dimensional data. The International Archives of the Photogrammetry, Remote Sensing and Spatial Information Sciences. 2008 Beijing ISPRS Vol. XXXVII. Part B2, pp. 1071–1076.

Cunningham, D., Grebby, S., Tansey, K., Gosar, A., Kastelic, V., 2006. Application of airborne LiDAR to mapping seismogenic faults in forested mountainous terrain, southeastern Alps, Slovenia. Geophysical Research Letter 33, L20308 http://dx.doi.org/10.1029/2006GL027014.

Harding, D.J., Berghoff, G.S., 2000. Fault scarp detection beneath dense vegetation cover: airborne LiDAR mapping of the Seattle fault zone, Bainbridge Island, Washington. Proceedings of the American Society of Photogrammetry and Remote Sensing Annual Conference, Washington, D.C. p. 9.

Haugerud, R.A., Harding, D.J., Johnson, S.Y., Harless, J.L., Weaver, C.S., Sherrod, B.L., 2003. High-resolution topography of the Puget Lowland, Washington — a bonanza for earth science. GSA Today 13, 4–10.

Hilley, G.E., Arrowsmith, J.R., 2008. Geomorphic response to uplift along the Dragon's Back pressure ridge, Carrizo Plain, California. Geology 36, 367–370.

Hilley, G.E., DeLong, S., Prentice, C., Blisniuk, K., Arrowsmith, J.R., 2010. Morphologic dating of fault scarps using Airborne Laser Swath Mapping (ALSM) data. Geophysical Research Letters 37, L04301 http://dx.doi.org/10.1029/2009GL042044.

Japan Meteorological Agency, 1971. The Climatic Atlas of Japan. Japan Meteorological Agency, Tokyo (in Japanese).

Kaneda, H., Okada, A., 2008. Long-term seismic behavior of a fault involved in a multiple-fault rupture: insights from tectonic geomorphology along the Neodani Fault, central Japan. Bulletin of the Seismological Society of America 98, 2170–2190.

Kondo, H., Toda, S., Okamura, K., Takada, K., Chiba, T., 2008. A fault scarp in an urban area identified by LiDAR survey: a case study on the Itoigawa–Shizuoka Tectonic Line, central Japan. Geomorphology 101, 731–739.

Lin, Z., Kaneda, H., Mukoyama, S., Asada, N., Chiba, T., 2009. Detection of small tectonic–geomorphic features beneath dense vegetation covers in Japanese mountains from high-resolution LiDAR DEM. Seismological Research Letters 80, 311–312.

Matsuda, T., 1974. Surface Faults Associated with Nobi (Mino–Owari) Earthquake of 1891, 13. Special Bulletin Earthquake Research Institute, University of Tokyo, Japan, pp. 85–126 (in Japanese, with English abstract).

National Institute of Advanced Industrial Science and Technology (AIST), 2009. Report on Improving Technique for Evaluation of Active Blind Faults Based on Tectonic Geomorphology. Japan Nuclear Energy Safety Organization, Tokyo (in Japanese, with English abstract).

Nelson, A.R., Johson, S.Y., Kelsey, H.M., Wells, R.E., Sherrod, B.L., Pezzopane, S.K., Bradley, L., Koehler, R.D., Buchnam, R.C., 2003. Later Holocene earthquakes on the Toe Jam Hill Fault, Seattle fault zone, Bainbridge Island, Washington. Geological Society of America Bulletin 115, 1388–1403.

Okada, A., Matsuda, T., 1992. Late Quaternary activity of the Neodani (Neo-Valley) Fault at Midori and Naka, Neo Village, central Japan. Journal of Geography (Tokyo) 101, 19–37 (in Japanese, with English abstract).

Oskin, M.E., Arrowsmith, J.R., Corona, A.H., Elliott, A.J., Fletcher, J.M., Fielding, E.J., Gold, P.O., Gonzalez-Garcia, J.J., Hudnut, K.W., Liu-Zeng, J., Teran, O.J., 2012. Near-field deformation from the E1 Mayor–Cucapah earthquake revealed by differential LiDAR. Science 335, 702–705.

Prentice, C.S., Crosby, C.J., Harding, D.J., Haugerud, R.A., Merritts, D.J., Gardner, T., Koehler, R.D., Baldwin, J.N., 2003. Northern California LiDAR data: a tool for mapping the San Andreas Fault and Pleistocene marine terraces in heavily vegetated terrain. Eos Transaction AGU 84 (46) Fall Meeting Supplement, Abstract G12A-06.

Sherrod, B.L., Brocher, T.M., Weaver, C.S., Bucknam, R.C., Blakely, R.J., Kelsey, H.M., Nelson, A.R., Haugerud, R.A., 2004. Holocene fault scarps near Tacoma, Washington, USA. Geology 32, 9–12.

Wechsler, N., Rockwell, T.K., Ben-Zion, Y., 2009. Application of high resolution DEM data to detect rock damage from geomorphic signals along the central San Jacinto Fault. Geomorphology 113, 82–96.

Yokoyama, R., Shirasawa, M., Kikuchi, Y., 1999. Representation of topographical features by opennesses. Journal of the Japanese Society of Photogrammetry and Remote Sensing 38, 26–34 (in Japanese, with English abstract).

Yokoyama, R., Shirasawa, M., Rike, R.J., 2002. Visualizing topography by openness: a new application of image processing to digital elevation models. Photogrammetric Engineering & Remote Sensing 68, 257–265.

Yoshioka, T., Awata, Y., Shimokawa, K., Ishimoto, H., Yoshimura, M., Matsuura, K., 2002. Paleoseismicity of the Nukumi Fault ruptured during the 1891 Nobi earthquake, central Japan, revealed by a trenching study. Journal of the Seismological Society of Japan 55, 301–309 (in Japanese, with English abstract).

Zachariasen, J., 2008. Detail mapping of the northern San Andreas Fault using LiDAR imagery. Final Technical Report of National Earthquake Hazards Reduction Program, pp. 1–47.

Zielke, O., Arrowsmith, R., Ludwig, L.G., Akciz, S.O., 2010. Slip in the 1857 and earlier large earthquakes along the Carrizo Plain, San Andreas Fault. Science 327, 1119–1122.